

RESEARCH ARTICLE

10.1002/2016JB013769

Ambient noise tomography across Mount St. Helens using a dense seismic array

Yadong Wang¹ , Fan-Chi Lin¹, Brandon Schmandt² , and Jamie Farrell¹¹Department of Geology and Geophysics, University of Utah, Salt Lake City, Utah, USA, ²Department of Earth and Planetary Sciences, University of New Mexico, Albuquerque, New Mexico, USA

Key Points:

- Ambient noise Rayleigh wave tomography was applied across a dense array at Mount St. Helens
- Biases introduced by inhomogeneous noise source are mitigated by azimuthal traveltimes correction
- Low-velocity anomaly due to the high-porosity volcanic edifice and shallowest extent of the magmatic system

Supporting Information:

- Supporting Information S1

Correspondence to:

Y. Wang,
yadong.wang@utah.edu

Citation:

Wang, Y., F.-C. Lin, B. Schmandt, and J. Farrell (2017), Ambient noise tomography across Mount St. Helens using a dense seismic array, *J. Geophys. Res. Solid Earth*, 122, doi:10.1002/2016JB013769.

Received 17 NOV 2016

Accepted 5 MAY 2017

Accepted article online 7 MAY 2017

Abstract We investigated upper crustal structure with data from a dense seismic array deployed around Mount St. Helens for 2 weeks in the summer of 2014. Interstation cross correlations of ambient seismic noise data from the array were obtained, and clear fundamental mode Rayleigh waves were observed between 2.5 and 5 s periods. In addition, higher-mode signals were observed around 2 s period. Frequency-time analysis was applied to measure fundamental mode Rayleigh wave phase velocities, which were used to invert for 2-D phase velocity maps. An azimuth-dependent traveltimes correction was implemented to mitigate potential biases introduced due to an inhomogeneous noise source distribution. Reliable phase velocity maps were only obtained between 3 and 4 s periods due to limitations imposed by the array aperture and higher-mode contamination. The phase velocity tomography results, which are sensitive to structure shallower than 6 km depth, reveal an ~10–15% low-velocity anomaly centered beneath the volcanic edifice and peripheral high-velocity anomalies that likely correspond to cooled igneous intrusions. We suggest that the low-velocity anomaly reflects the high-porosity mixture of lava and ash deposits near the surface of the edifice, a highly fractured magmatic conduit and hydrothermal system beneath the volcano, and possibly a small contribution from silicate melt.

1. Introduction

Mount St. Helens (MSH) is an active basalt-through-dacite volcano located in southwest Washington State within the Cascades magmatic arc, which is driven by subduction of the Juan de Fuca Plate beneath western North America (Figures 1a and 1b). Volcanism at MSH has been active since ~300 ka [Clyne *et al.*, 2008]. A Plinian eruption occurred in May 1980 in concert with a massive landslide on the northern flank of the volcanic edifice [Lipman and Mullineaux, 1981]. Within the resulting summit crater, resurgent lava dome growth occurred from 1980 to 1986 [Swanson *et al.*, 1987]. Eruptive activity then ceased until October 2004, when dome growth continued with extrusion of a dacite plug accompanied by abundant shallow seismicity from 2004 to 2008 [Sherrod *et al.*, 2008; Waite *et al.*, 2008; Thelen *et al.*, 2008]. Since 1980, there have been a variety of multidisciplinary studies of magmatic processes and the subsurface structure at MSH.

In the field of seismology, significant progress has been made in seismic imaging of the MSH magmatic system with body wave traveltimes tomography [e.g., Lees, 1992; Moran *et al.*, 1999; Waite and Moran, 2009; Kiser *et al.*, 2016]. Waite and Moran [2009] produced high-resolution *P* wave velocity models for the uppermost 10 km and found evidence for major features of the magmatic system including very low velocities within the volcanic edifice, a shallow magma reservoir at ~2–3 km below sea level, high velocities corresponding to peripheral intrusions, and perhaps the top of a larger magma reservoir at depths greater than ~7 km. Before 2014, most seismic studies used natural earthquake data recorded by the Pacific Northwest Seismic Network (PNSN) and Cascades Volcano Observatory seismic networks, which consists of 12 stations within 10 km of MSH with a mix of vertical-component short-period seismographs, three-component short-period borehole seismographs, and three-component broadband seismographs (<http://www.pnsn.org>).

From 2012 to 2016, the seismic data collection portion of the iMUSH (Imaging Magma Under St. Helens) project, a collaborative project to study the magmatic system in the MSH area, was carried out. During the iMUSH project, a variety of multiscale seismic data were obtained including the following: an active source experiment with a total of 23 explosive sources and ~5000 geophone recording sites [Kiser *et al.*, 2016], continuous recording by 70 broadband seismographs from 2014 to 2016 [Ulberg, 2015; Crosbie, 2015], and a 2 week deployment of 904 continuously recording geophones within 15 km of MSH [Hansen and Schmandt, 2015]. Existing products from the ongoing research project include 2-D traveltimes tomography of the crust

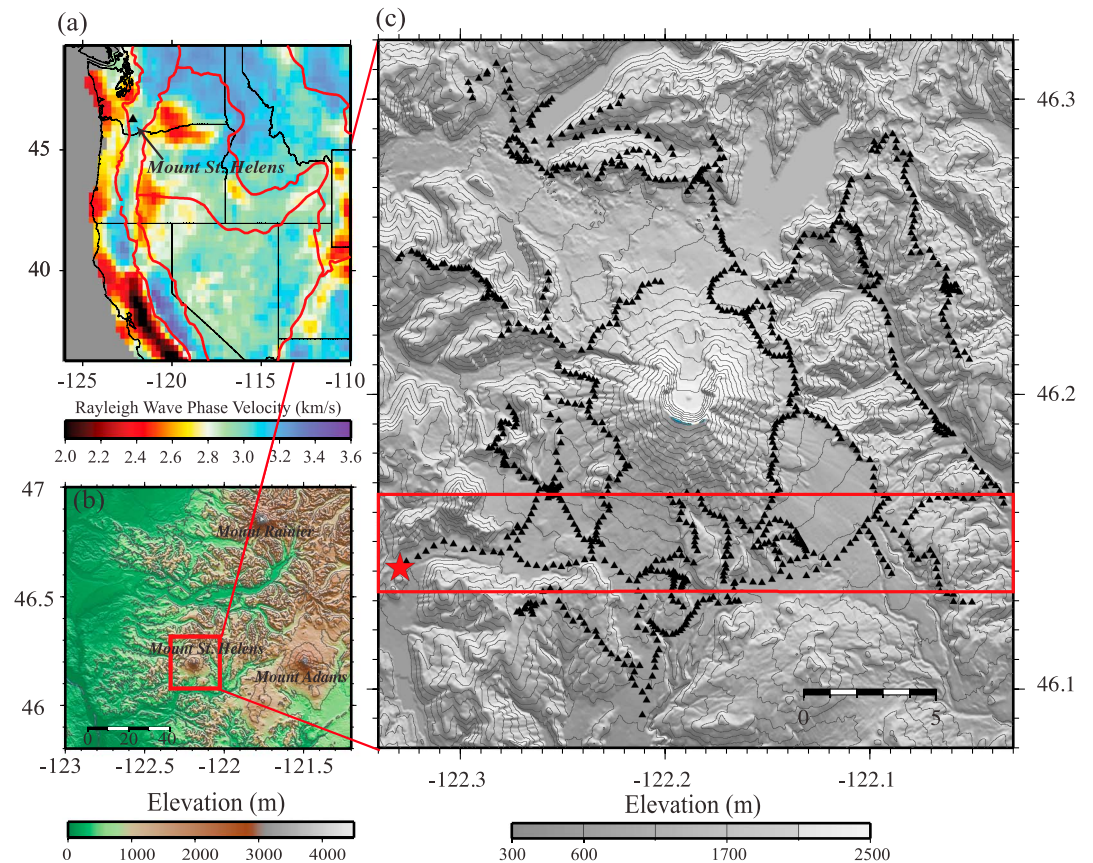


Figure 1. (a) The 5 s Rayleigh wave phase velocity map of the western United States [Ekström, 2014] and the location of the Mount St. Helens (MSH). (b) Topography of MSH and surrounding area. (c) The MSH node array. The black triangles are MSH node array stations. The red star and red box are used in Figure 2.

[Kiser *et al.*, 2016], reflection imaging of the Moho [Hansen *et al.*, 2016], and detection and location of local microseismicity [Hansen and Schmandt, 2015]. New structural imaging based on the iMUSH data has so far focused on depths greater than ~ 4 km. Kiser *et al.* [2016] found evidence for an upper crustal magma reservoir at ~ 4 – 13 km below sea level directly beneath the MSH and a lower crustal reservoir offset to the southeast of MSH by about 20 km. In this study, we use the 2 weeks of continuous data recorded by the 904 cable-free geophones (Figure 1c), referred to as nodes, to investigate the upper crust with ambient noise interferometry.

Ambient noise surface wave tomography has now been widely used to image subsurface structure [e.g., Shapiro *et al.*, 2005; Yao *et al.*, 2008; Lin *et al.*, 2008, 2013; Ekström, 2014; Ward, 2015; Zigone *et al.*, 2015]. The general process of determining the empirical Green's functions from noise cross correlations and measuring surface wave dispersion using frequency-time analysis is well documented [Bensen *et al.*, 2007; Lin *et al.*, 2008]. While most ambient noise tomography studies use broadband seismometers to extract surface wave signals between the microseismic period band (~ 6 – 30 s periods) for regional- to continental-scale crust and upper mantle studies [e.g., Lin *et al.*, 2008; Yao *et al.*, 2008; Moschetti *et al.*, 2010], recent studies based on dense geophone arrays have also demonstrated the possibility to extract shorter-period surface waves for local and shallow crustal imaging [de Ridder and Dellinger, 2011; Lin *et al.*, 2013; Roux *et al.*, 2016]. Apart from surface waves, recent ambient noise studies have also demonstrated the possibility of retrieving body waves using cross correlations [e.g., Draganov *et al.*, 2009; Zhan *et al.*, 2010; Ruigrok *et al.*, 2011; Poli *et al.*, 2012a, 2012b; Lin *et al.*, 2013; Nakata *et al.*, 2015, 2016].

In this study, we performed ambient noise Rayleigh wave tomography across the iMUSH dense seismic array in the MSH area (Figure 1c). To our knowledge, this is the first time ambient noise tomography has been applied on a dense array with a ~ 25 km aperture. Moreover, instead of a roughly uniform 2-D surface grid,

the array was deployed along available trails, which makes it impossible to use array tomography methods such as eikonal tomography [Lin *et al.*, 2009]. This new array geometry and scale raises some questions regarding limitations on the applicability of ambient noise surface wave tomography. First, it is unclear if it is possible to extract robust surface wave measurements using 10 Hz geophones on a 25 km scale. As high-frequency surface waves tend to scatter and attenuate in short distances and instrument sensitivity drops quickly below the corner frequency, the frequency band with useful signal, if any, is likely limited. Second, the noise environment below the microseismic period band (<6 s) in this area is unknown. For instance, it is unclear if the noise wavefield is mostly oceanic related. Finally, it is unknown if the noise sources are adequately distributed at different azimuths to produce unbiased empirical Green's functions [Snieder, 2004].

We address the challenges mentioned above by performing careful ambient noise surface wave analyses. We demonstrate that it is possible to extract Rayleigh wave signals between ~ 2.5 and 5 s periods from noise cross correlations using a 25 km aperture 10 Hz geophone dense array but that a higher-mode signal dominates at 2 s. We also demonstrate that the seismic noise sources can be significantly unevenly distributed in this period band such that an azimuthally dependent traveltimes correction is needed to mitigate the potential tomographic biases. Finally, we show that our Rayleigh wave phase velocity tomography results provide new constraints to the shallow magmatic and hydrothermal system beneath the MSH.

2. Data and Method

We used continuous ambient seismic noise data recorded by 904 vertical-component short-period nodes deployed between 18 July 2014 and 5 August 2014 near the edifice of MSH. The nodes were mostly deployed along available trails and rural roads, and the full aperture of the array was about 25 km with ~ 0.3 km station spacing (Figure 1c). Each node contains a vertical component geophone. Although the corner frequency of the geophone is 10 Hz, Lin *et al.* [2013] have demonstrated that similar instruments can observe usable signals at least up to 2 s period across the Long Beach array, and the long-period limitation is mostly due to the dense array configuration and the far-field requirement [Yao *et al.*, 2006]. As the ~ 25 km aperture of the MSH array used in this study is larger than the Long Beach array, it is possible to extend the signal extracted from noise cross correlations to higher periods.

2.1. Noise Cross Correlation

We closely followed the method described by Lin *et al.* [2013] to calculate ambient noise cross correlations between each station pair. First, the noise data were cut into 1 h segments, their spectra were whitened, and all possible interstation cross correlations were computed. Then each 1 h cross correlation was normalized by its maximum amplitude to suppress the effects of earthquakes and other coherent signals. All available normalized cross correlations for each station pair were stacked to obtain the final interstation cross correlation. About 0.4 million ($\sim 904^2/2$) cross correlations were obtained across the MSH node array.

Figure 2 shows an example record section of cross correlations between a virtual source station in the west and all receiver stations to the east (Figure 1c). Clear energy moveout is observed on the positive time lag between 1 and 10 s periods (Figure 2a). No clear signal is observed on the negative time lag suggesting that the ambient noise wavefield is mostly excited by the ocean-solid earth interaction in the west [Traer *et al.*, 2012]. We roughly estimated the average phase velocities by measuring the slopes of the phase moveout in Figure 2. Between 2.5 and 5 s periods (Figure 2c), a phase velocity near 2.7 km/s is observed, which is consistent with the previous fundamental mode Rayleigh wave phase velocity measurements in the area obtained through larger-scale broadband networks (Figure 1a) [Ekström, 2014]. Between 1.5 and 2.5 s periods (Figure 2b), the observed phase moveout is significantly faster with a phase velocity near 4.2 km/s similar to the mantle shear velocity. This observation indicates that this signal is more likely related to higher-mode surface waves instead of fundamental Rayleigh waves. Further analysis (see section 4.3) supports this assumption. In this study, we focused on performing tomography using the fundamental mode Rayleigh wave phase measurements as the higher-mode signals are dominantly observed within a relatively narrow range of azimuthal directions.

Recently, using data from the Japanese Hi-net seismic network, Takagi *et al.* [2015] demonstrated that a 1 s repeating instrument noise signal, likely related to GPS timing calibration, can potentially contaminate

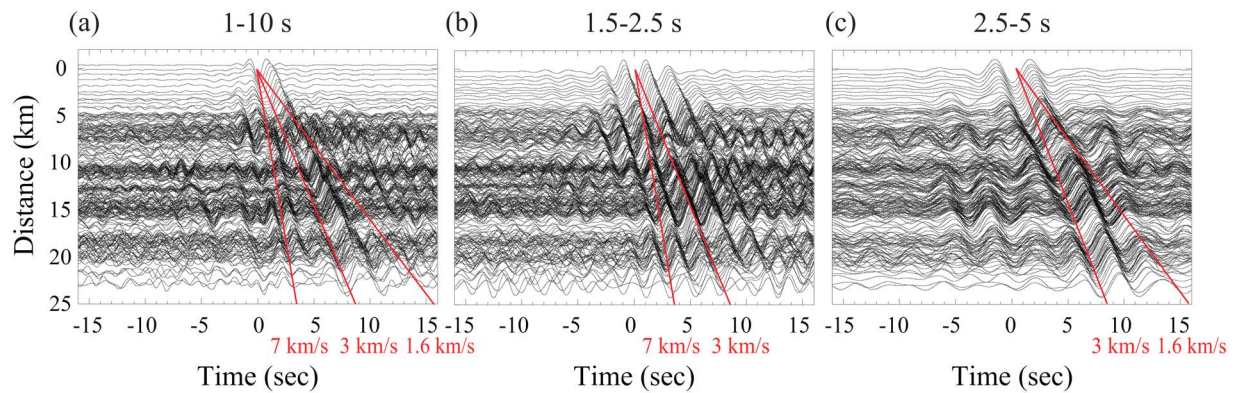


Figure 2. The record section of cross correlations calculated between a center station (red star in Figure 1) and stations on a west-east zone (red box in Figure 1). (a–c) Results 1–10 s band passed, 1.5–2.5 s band passed, and 2.5–5 s band passed, respectively.

ambient noise cross correlations. As the GPS calibration is coherent across the entire array, such instrument noise will result in repeating 1 s spikes in the noise cross correlations. While we do not observe such a signal in our single-pair cross correlations, the signal is present after stacking our cross correlations using distance bins (Figure 3a). Similar to *Takagi et al.* [2015], we can also observe the instrument noise signal directly by stacking raw noise records (Figure 3b). To mitigate the potential effect of this artificial signal, we corrected all of our single-pair cross correlations by using a spike template constructed from the spike signals observed in our stacked cross correlations (Figure 3a). We calculated the amplitude of the template with the assumption that the instrument noise is station and time independent. While the process did not alter single-pair cross correlations in a major way, it successfully removed the artificial spike signals in the stacked cross correlation, including when band passed near 1 Hz frequency (Figures 3c and 3d). The remainder of the paper focuses on the results from spike-removed cross correlations.

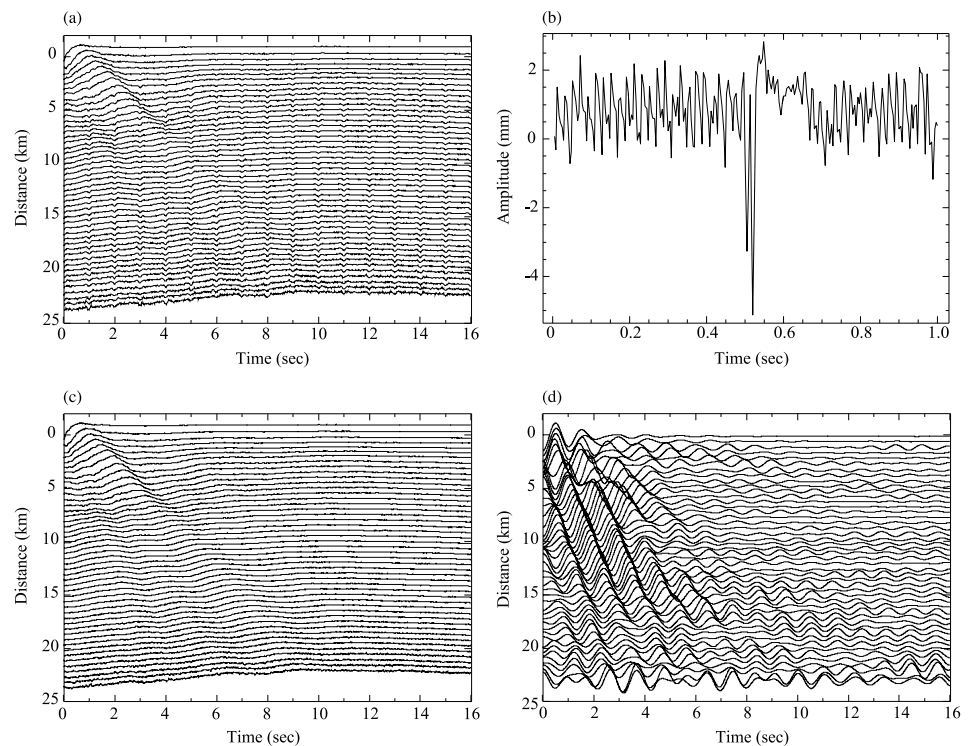


Figure 3. (a) Stacked cross correlations in 0.5 km distance bins without band pass. (b) Stacked 1 s raw noise data, shifted by 0.5 s. (c) Stacked cross correlations after removing the 1 Hz spikes without band pass. (d) Same as Figure 3c but band passed 0.8–1.2 s.

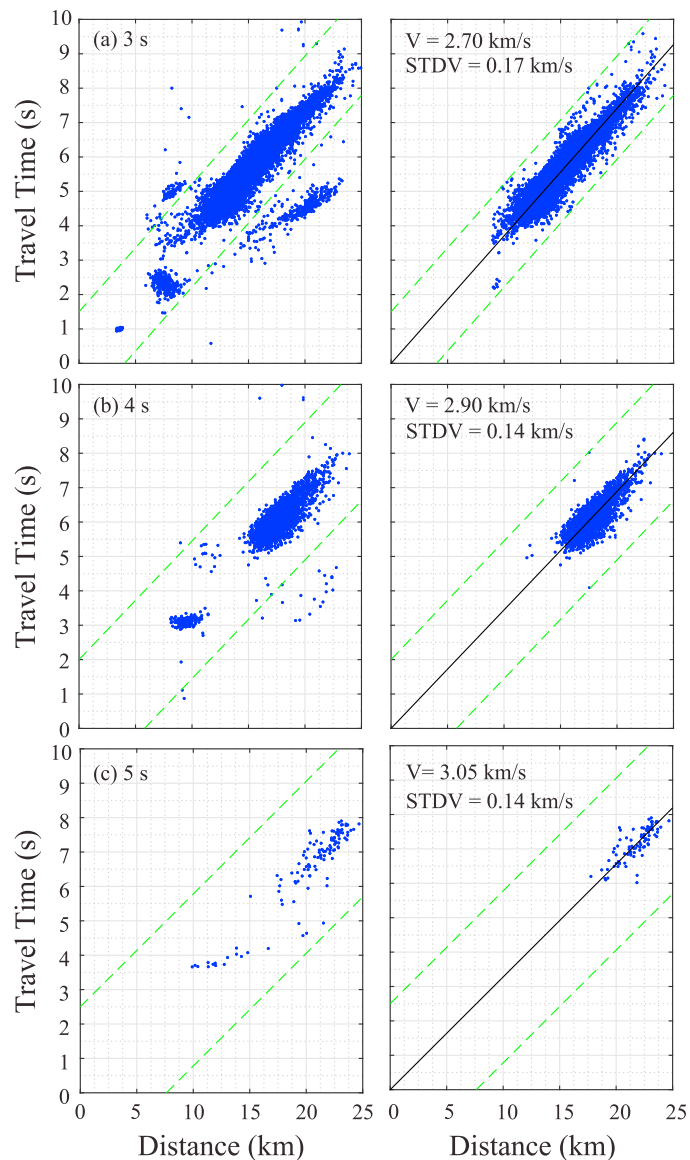


Figure 4. Phase traveltimes versus distance for 3, 4, and 5 s Rayleigh waves satisfying the SNR and group velocity selection criterion (left). Blue dots are the measurements. Green dashed lines are the boundaries of phase ambiguity correction. The measurements applied phase ambiguity correction and one-wavelength distance selection criterion (right). The black lines fit the measurements by minimizing the misfit of traveltimes. The mean and the standard deviation of the velocity are noted in the figure.

2.2. Rayleigh Wave Phase Traveltimes

We measured the phase velocities of the Rayleigh waves between 2.5 and 5 s by automated frequency-time analysis [Bensen *et al.*, 2007; Lin *et al.*, 2008]. To reduce the effect of source inhomogeneity and potentially improve the signal-to-noise ratio (SNR) particularly for those station pairs that are not aligned with the oceanic direction, we averaged the positive and negative lags of the cross correlations to obtain symmetric cross correlations. While in principle we can measure the signals on the positive and negative lags separately [e.g., Zigone *et al.*, 2015], we do not expect that such a process will alter our result significantly. To evaluate the SNR of the cross-correlation signals, we assumed a 1.6–5 km/s velocity range for Rayleigh waves. Both leading and trailing SNRs were calculated, where the SNRs were defined as the ratio between the maximum amplitude within the signal window to the root-mean-square (RMS) amplitudes within the noise windows. In general, on top of random incoherent noise, the leading SNR can be affected by the presence of body waves and higher-mode signals, while the trailing SNR can be affected by reflected/coda waves. In this study, we used

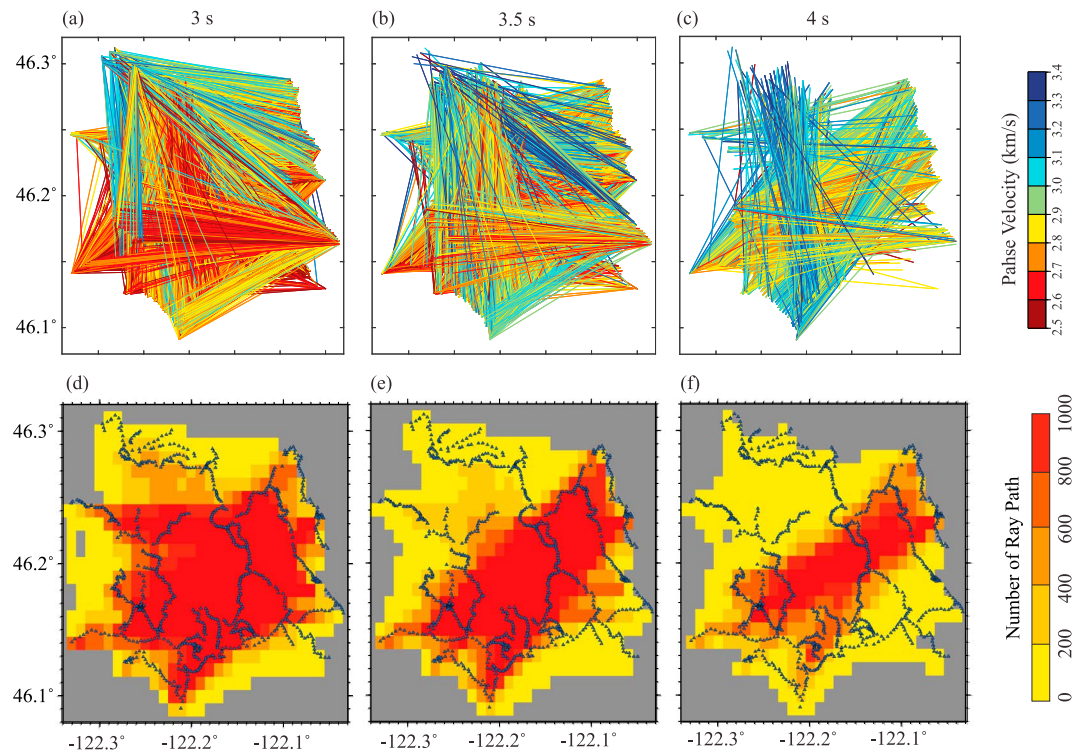


Figure 5. (a–c) Rayleigh wave phase velocity measurements for 3, 3.5, and 4 s periods. (d–f) Ray coverage density maps for 3, 3.5, and 4 s periods.

SNR > 4 as a criterion for both leading and trailing SNRs to select good measurements. In addition to the SNR criterion, we also imposed a period-dependent maximum group velocity (3.0 km/s for periods <4.5 s and 3.3 km/s for periods ≥4.5 s) to separate fundamental from higher-mode Rayleigh waves. The group velocity criterion is determined based on the predicted group velocity dispersion curve of the fundamental Rayleigh waves from a 1-D model described in section 4.3.

Figure 4 shows all Rayleigh wave phase traveltimes as a function of distance at 3, 4, and 5 s periods satisfying the SNR and group velocity selection criterion. To mitigate the potential phase traveltimes biases due to 2π ambiguity [Lin *et al.*, 2008], we first used all measurements to estimate a reference phase velocity for each period. We then corrected all phase traveltimes measurements by N periods (N is an integer) such that the difference between the predicted and observed traveltimes is less than a half period. To only retain the most reliable measurements, we further imposed a one-wavelength far-field selection criterion to avoid significant bias due to near-field effects [Lin *et al.*, 2013]. Note that the one-wavelength criterion imposed in this study is less strict compared to the two to three wavelengths suggested in earlier broadband studies [e.g., Yao *et al.*, 2006; Bensen *et al.*, 2007]. Because of the limited aperture of the dense array, selecting a stricter far-field criterion would significantly reduce the number of measurements and deteriorate the quality of the tomography results.

Figure 5 shows the phase velocity measurements and ray coverage maps for the 3, 3.5, and 4 s Rayleigh waves. The ray coverage maps show that the edifice of MSH is well covered by raypaths for these three periods. While phase velocities are generally slower for raypaths crossing the center of our study area for 3 and 3.5 s periods, large variations are observed for measurements with different orientations particularly at 4 s period. We will discuss these observed spatial and azimuthal variations in detail in the following sections. At longer periods, both the instrument response of the geophones and the array aperture limited the number of measurements available for tomography. At shorter periods, the interference between higher-mode Rayleigh waves made it challenging to isolate the fundamental mode Rayleigh waves (Figure 2b).

We used the 2-D tomographic method of Barmin *et al.* [2001] to invert for 2-D Rayleigh wave phase velocity maps on a $0.01^\circ \times 0.01^\circ$ grid. The method is derived using ray theory, and the inversion is regularized by both

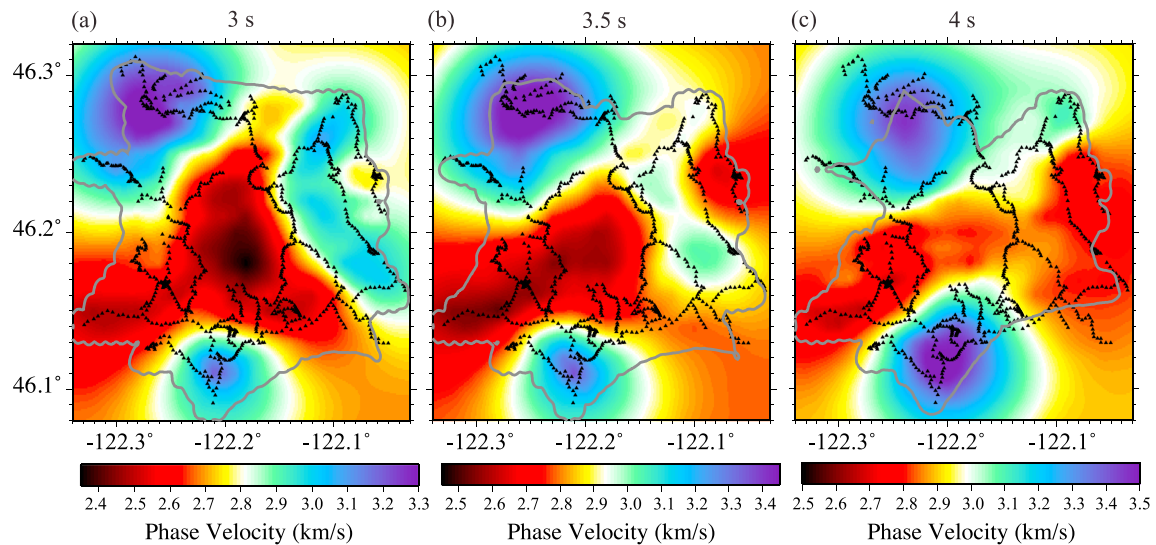


Figure 6. (a–c) The 3, 3.5, and 4 s Rayleigh wave phase velocity maps. Black triangles represent seismic stations. Contours enclose the region with >20 /grid ray coverage.

smoothing and damping parameters. The determination of the regularization parameters is somewhat empirical. However, tests using different regularization parameters show very similar results for areas with good data coverage. Despite the extremely high raypath density (Figure 5), we did not try to resolve structure smaller than ~ 5 km, which is approximately half of the Rayleigh wave wavelength used in this study.

3. Tomography Results

Figure 6 shows the inverted Rayleigh wave phase velocity maps at 3, 3.5, and 4 s periods. A clear low-velocity anomaly is observed at 3 s period centered beneath the MSH edifice, which is surrounded by relatively high velocity anomalies. At 3.5 and 4 s periods, the slow anomaly gradually degrades and the shape of the anomaly gradually becomes east-northeast to west-southwest elongated. At 4 s, assuming 3 km/s phase velocity, Rayleigh waves have a wavelength near 12 km. Considering the aperture of the array, almost all the measurements used in the 4 s inversion are between one and two wavelengths. As traveltime measurements within a couple wavelengths are very sensitive to the heterogeneous distribution of noise sources [Yao and van der Hilst, 2009], the elongated anomaly may be an artifact due to unaccounted biases of seismic interferometry.

To evaluate and mitigate the potential biases due to inhomogeneous noise source distribution, we analyzed the residual traveltime distribution using back azimuth and distance for 3, 3.5, and 4 s Rayleigh waves. The residuals were calculated based on a constant reference velocity. As the biases could already affect the inverted tomography maps, the residuals after inversion would not reflect the true bias. For the three periods of interest, the azimuthal and distance bin-averaged residual distributions are summarized in Figures 7a–7c. The residual distribution is symmetric across 180° rotation as all measurements are from the symmetric components of the cross correlations. The residual distribution is clearly azimuthally dependent, where systematic positive traveltime residuals (slower than predicted) are observed in the east-northeast to west-southwest direction similar to the elongated slow anomaly observed in our 3.5 and 4 s tomography maps (Figures 6b and 6c).

To confirm the relationship between the residual distribution and noise source distribution, we performed azimuthal and slowness beamforming [e.g., Harmon et al., 2008] to determine the propagation intensity of the noise wavefield in different directions at 2, 3, and 4 s periods (Figures 7d–7f). To perform time domain beamforming, for each 1° back azimuthal bin and each assume slowness, we first stacked all available cross correlations corrected by the predicted traveltime. The stacked cross correlation is then normalized by the number of cross correlations before the maximum amplitude is taken as the beam intensity. We used all of our nonsymmetric cross correlations for beamforming so that the true propagation direction can be evaluated. At all three periods, strong signals coming from the west-southwest direction are observed

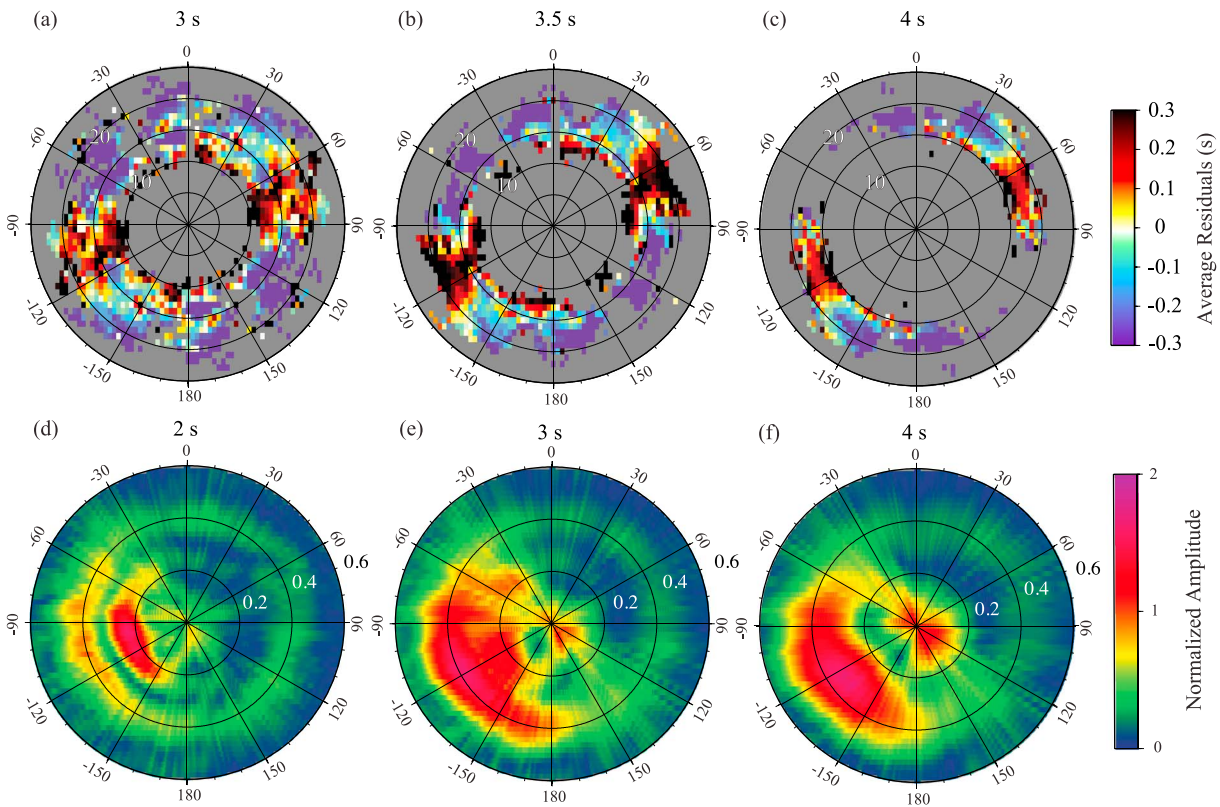


Figure 7. (a–c) Back azimuth versus distance (0–25 km) plots of residual distributions for 3, 3.5, and 4 s Rayleigh wave measurements. (d–e) Back azimuth versus phase slowness plots of beamforming of all the cross correlations for 2, 3, and 4 s periods. Slowness is the radial distance on the polar plots from 0 to 0.6 s/km.

suggesting that the dominant noise signals are likely related to the interaction between the Pacific Ocean and the Oregon coastline. At 2 s, both Rayleigh wave and higher-mode signals can be identified where the higher-mode signal with slowness < 0.3 s/km is significantly stronger. This is consistent with the cross-correlation record section shown earlier (Figure 2) and again explains why it is difficult to obtain good Rayleigh wave measurements below 3 s period. At longer periods, the higher-mode signal gradually reduces in strength and the Rayleigh wave becomes the dominant signal.

The clear correlation between the traveltime residual distribution and beamforming results (Figure 7) indicates that the azimuthal traveltime bias is due to inhomogeneous source distribution. When a raypath is parallel to the dominant noise propagation direction, the phase traveltime measurement is expected to be slower than its theoretical value [Lin *et al.*, 2008; Yao and van der Hilst, 2009]. This is because the time interval is longest for a wave propagating through two stations when the wave propagation direction is parallel to the raypath. To construct the exact Green’s function, homogeneous source distribution is required particularly within the constructive interference areas [Snieder, 2004]. When the sources are only presented along the extended line connecting the two stations, the cross correlation will have a $\pi/4$ phase delay compared to when noise sources are homogeneously distributed [Lin *et al.*, 2008].

To remove this apparent noise source bias, we empirically determined the trend of the azimuthally dependent bias. For each 20° azimuthal bin, we calculated the mean and standard deviation of the mean of all traveltime residuals (Figure 8). We then determined a traveltime correction function f for each period using least squares fitting. Here we used a Fourier expansion with up to 90° periodicity

$$f(\theta) = a + b \cos(2\theta) + c \sin(2\theta) + d \cos(4\theta) + e \sin(4\theta), \quad (1)$$

where $a, b, c, d,$ and e are expansion coefficients and θ is the back azimuth. We ignored the odd θ terms due to the 180° symmetry of the traveltime residual.

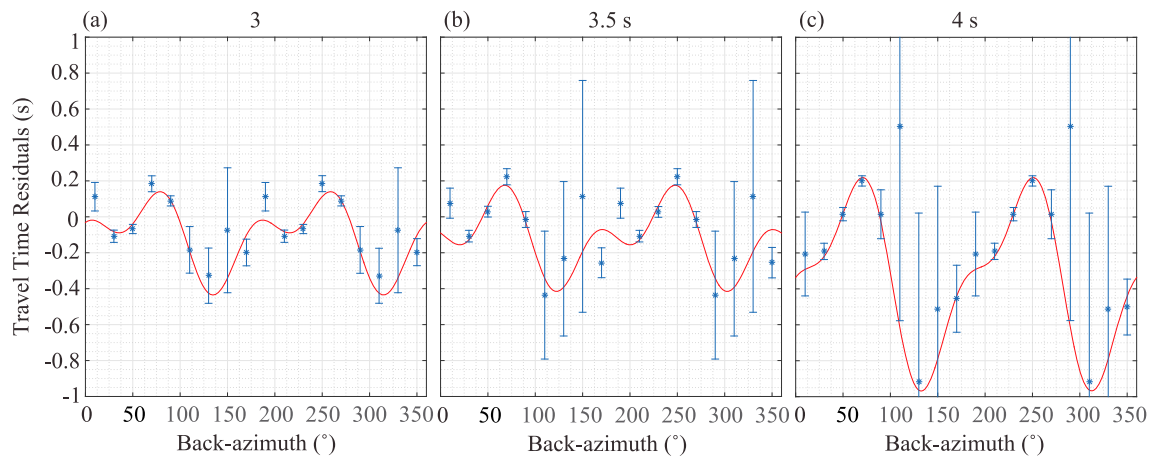


Figure 8. Traveltime residuals versus back azimuth for 3, 3.5, and 4 s Rayleigh wave measurements. The mean values of the residuals and standard deviations of the mean (enlarged by 5 times) in 20° bins are shown with stars and error bars. The red curves represent the best fitting curves based on equation (1).

We applied the azimuthal correction function to all of our traveltime measurements and then performed another round of tomography inversion (Figures 9a–9c). Compared to the results without azimuthal correction, the apparent elongation of the slow anomaly in the west-southwest to east-northeast direction at 3.5 and 4 s periods is suppressed. The low-velocity anomaly beneath the MSH crater observed at all three periods correlates well with the volcano edifice and the most active seismicity area (Figure 9d). Notice that one of the drawbacks of the azimuthal correction is that we can no longer investigate azimuthal anisotropy with the traveltime measurements.

To evaluate the tomography result quantitatively, Figure 10 shows the traveltime residual distribution before (left column) and after the inversion without (middle column) or with (right column) azimuthal correction. About 40–50% variance reduction is achieved at the three periods after the inversion where the standard deviation (SD) traveltime residual reduced from ~0.3 s to ~0.17 s. Supporting information Figure S1 shows the residual reduction for all raypaths. The overall residual only improves slightly for inversion after the azimuthal correction suggesting that azimuthal biases are not the dominant source of traveltime variance. The 0.17 s residual is about one twentieth of a period for the periods that we are interested in and may be close to the fundamental uncertainty of our phase traveltime measurements. To avoid the effect of obvious

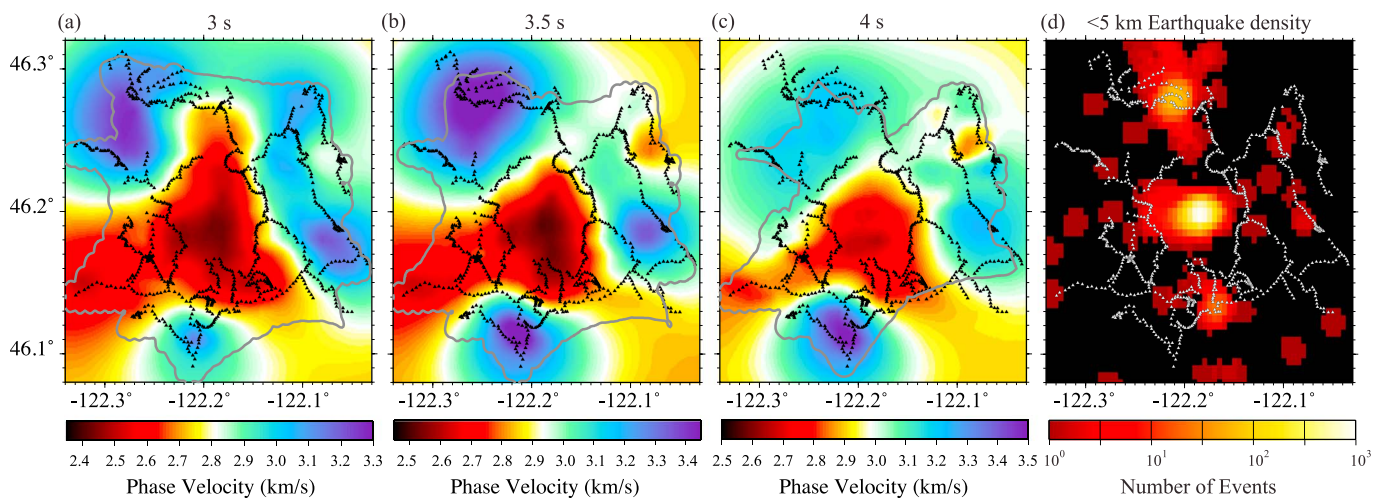


Figure 9. (a–c) The 3, 3.5, and 4 s Rayleigh wave phase velocity maps after azimuthal correction. Black triangles represent seismic stations. Contours enclose the region with >20/grid ray coverage. (d) The earthquake density map at MSH area, showing $M > 0$ earthquakes at <5 km depth from 2009 to 2016 cataloged by the PNSN (www.pnsn.org).

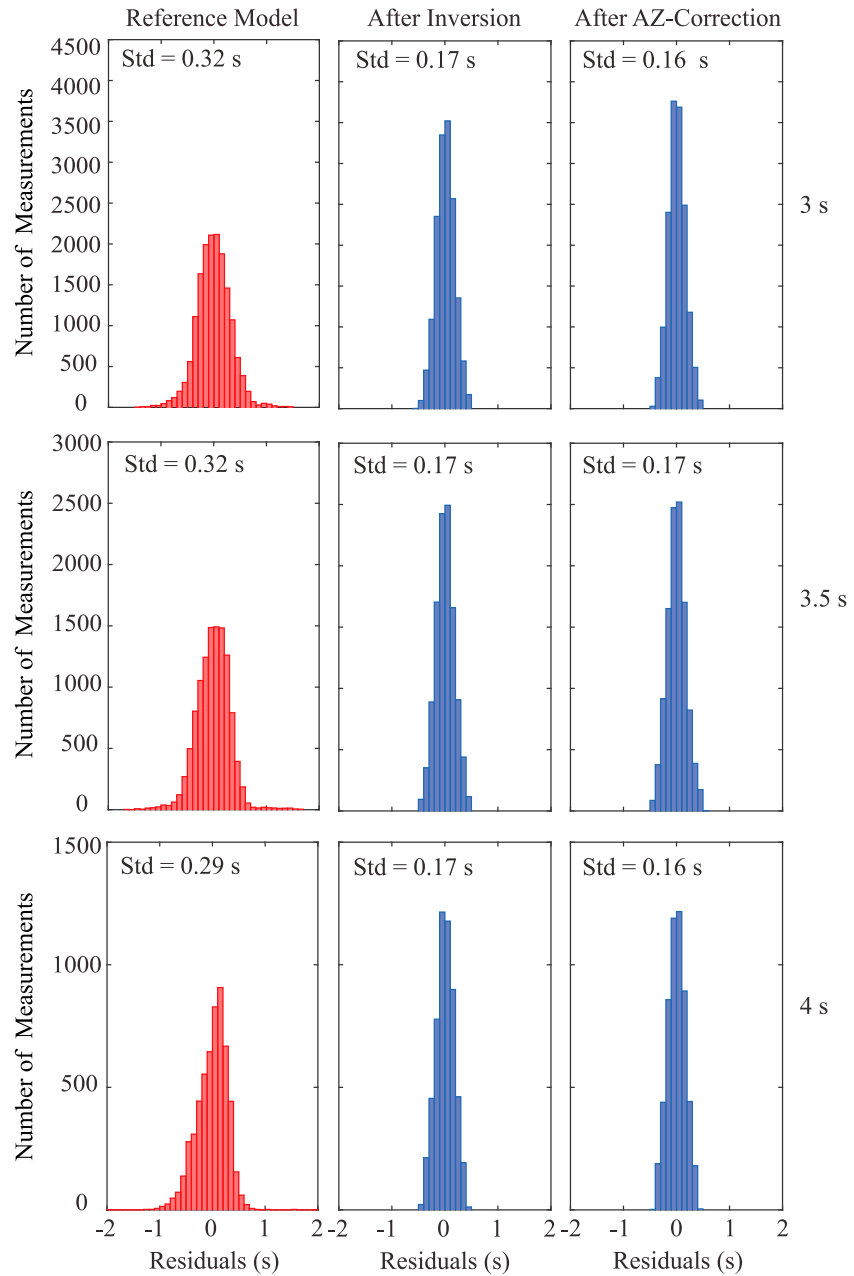


Figure 10. Traveltime residual distributions of 3, 3.5, and 4 s Rayleigh wave measurements. (left column) Residuals based on reference constant velocities. (middle column) Residuals based on tomography maps without azimuthal correction (Figure 6). (right column) Residuals based on tomography maps applied azimuthal correction (Figure 9).

outliers affecting our tomography result, we removed all traveltime measurements with residuals outside of 2 SD after inversion. We then performed a second tomography inversion. No noticeable difference was observed between the results of the first and second iterations.

4. Discussion

4.1. Depth Sensitivity

To evaluate the depth sensitivity of our phase velocity maps, we calculated the depth V_s sensitivity kernels of 3, 3.5, and 4 s Rayleigh waves based on the 1-D P and S wave velocity model from the active source study at

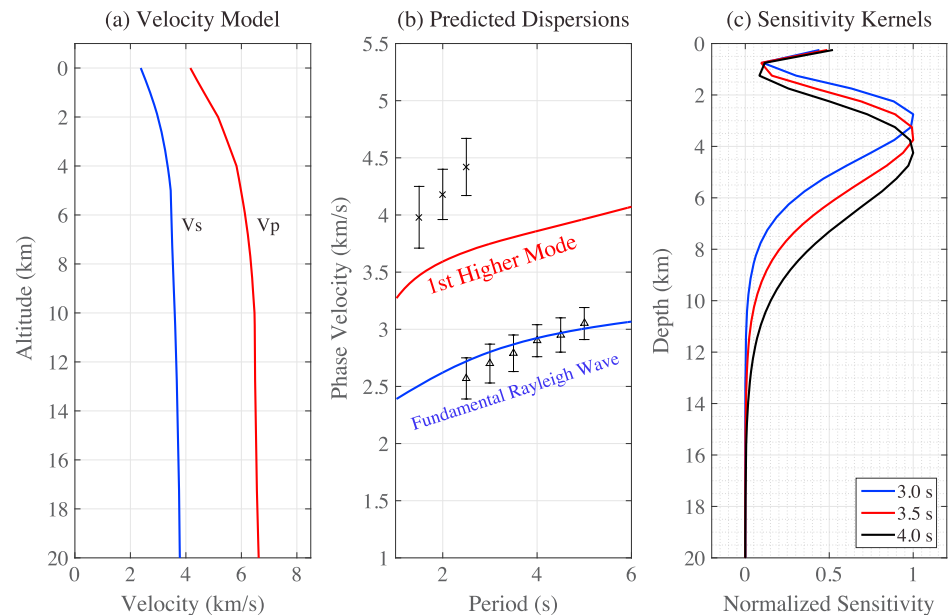


Figure 11. (a) The modified 1-D velocity model. (b) Predicted dispersion curves of the fundamental Rayleigh wave (blue) and the first higher mode (red). Black triangles are phase velocity measurements of the Rayleigh wave (Figure 4). Black crosses are the phase velocity measurements of the higher mode (Figure 13). Error bars are standard deviations of the velocity measurements. (c) The shear velocity sensitivity kernels of 3, 3.5, and 4 s Rayleigh waves.

MSH [Kiser *et al.*, 2016]. The density was determined by an empirical relationship between density and P wave velocity [Brocher, 2005]. We slightly modified the 1-D model by removing all shallow structure above sea level because the modified model better predicts the observed averaged Rayleigh wave dispersion measurements (Figure 11). The V_s sensitivity kernels were constructed by numerically calculating the partial derivative of the predicted phase velocity with respect to V_s model perturbation at different depths. While both V_p and density can also affect Rayleigh wave phase velocities, the sensitivity is considerably smaller. The sensitivity kernels of the Rayleigh waves (Figure 11c) show that 3, 3.5, and 4 s Rayleigh wave tomography maps (Figure 9) have peak sensitivity to subsurface structure at ~ 3 , ~ 3.5 , and ~ 4 km depths, respectively, and some sensitivity to the top 1 km structure. Average elevation of the array is ~ 1 km, so the peak sensitivity depths correspond to 2–3 km below sea level and most of the sensitivity is above ~ 5 km below sea level.

4.2. Volcanic Structure

Given the relatively shallow depth sensitivity, it is unlikely that the low-velocity anomaly imaged beneath the volcanic edifice is a manifestation of the main magma reservoir for the 1980 eruption, which is expected to be deeper than ~ 5 km based on petrology, seismicity, and surface deformation following the 1980 eruption, and a recently imaged high V_p/V_s volume [Pallister *et al.*, 2008; Scandone and Malone, 1985; Kiser *et al.*, 2016]. The depth resolution of the new Rayleigh wave results is quite limited, but the decrease in amplitude of the low-velocity anomaly from 3 to 4 s suggests that the low-velocity structure is prominent above ~ 3 km below sea level and fading by 4–5 km depth. Local earthquake V_p tomography of Waite and Moran [2009] found evidence for a small low-velocity anomaly at ~ 1 –3 km depth, which overlaps with but is more compact than the area of low 3–4 s Rayleigh wave phase velocities. Dacites from the 2004 eruption indicate that magma may have been temporarily staged at such shallow depths [Rutherford and Devine, 2008], and groundmass phenocrysts from the late stages of the 1980 eruption are consistent with some melt staging at similarly shallow depths [Cashman, 1992]. Additionally, there is evidence consistent with modest post-2008 magma recharge as the cause of rotated fault plane solutions [Moran *et al.*, 2014]. However, the compact, ~ 2 km in depth and ~ 3 km width, ~ 3 –5% low V_p anomaly imaged by Waite and Moran [2009] is an insufficient explanation for the larger area of ~ 10 –15% low Rayleigh wave phase velocity anomaly (Figure 9).

We suggest that the low phase velocities of ~ 2.3 – 2.7 km/s beneath the edifice (Figure 9) represent a relatively high porosity volume beneath the edifice due to the mixtures of lava and ash deposits near the surface and

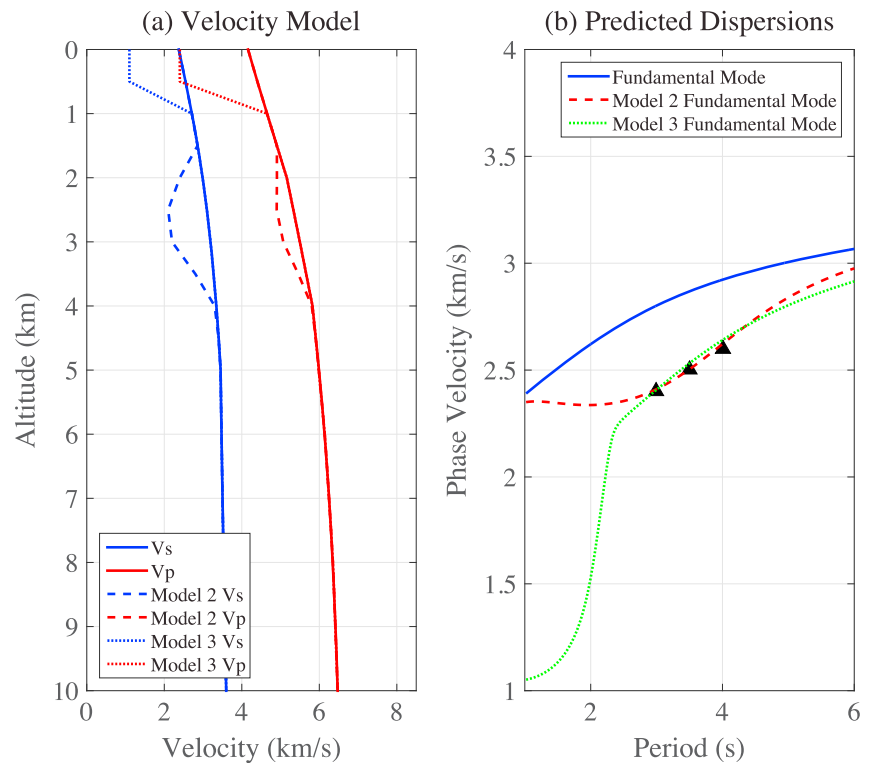


Figure 12. (a) Solid lines: the 1-D reference model shown in Figure 11a; dashed lines: the model 2 with a low-velocity layer at 1.5–4 km depth; and dotted lines: the model 3 with a low-velocity layer at top 1 km depth. (b) Predicted dispersion curves of the fundamental Rayleigh wave based on the reference model (blue solid line), model 2 (red dash line), and model 3 (green dotted line) shown in Figure 12a. Black triangles represent phase velocity tomography measurements at the center of MSH edifice for 3, 3.5, and 4 s periods.

the magmatic conduit and surrounding hydrothermal system. Near-surface velocities of volcanic edifices are known to be composed of highly fragmented lava and pyroclastic material and could have very low seismic velocities [Brenquier *et al.*, 2007; Masterlark *et al.*, 2010; Mordret *et al.*, 2015]. The presence of the hydrothermal system connected to the surface [Bedrosian *et al.*, 2007] also supports a high-porosity near-surface layer that could dramatically reduce shear velocities. Despite the weaker sensitivity near the surface (Figure 11), an ~50% velocity reduction in the top 1 km can potentially explain our tomographic observation (Figure 12).

Due to the poor depth resolution associated with our narrowband measurements, we cannot rule out the possibility of a contribution from a low-velocity anomaly between ~1.5–4 km depth (Figure 12). However, the concentration of <5 km deep earthquakes in the center of the low-velocity anomaly (Figure 9d) [Musumeci *et al.*, 2002; Waite and Moran, 2009; Hansen and Schmandt, 2015] indicates that rocks in this volume are capable of brittle failure and probably are not in the middle of a major reservoir of silicate melt. A small volume of silicate melt storage may exist adjacent to the vertical column of seismicity [Waite and Moran, 2009]. More spatially extensive contributions to the low-velocity anomaly could come from a highly fractured region beneath the volcanic edifice owing to stress reorganization above the >5 km deep volume from which magma was extracted during the 1980 eruption [Scandone and Malone, 1985; Pallister *et al.*, 2008]. Within this volume a deeper hydrothermal system driven by the ≥ 5 km magma reservoir may exist with limited connectivity to the near-surface system provided by continual fracturing within the subvertical column of upper crustal seismicity [e.g., Hurwitz *et al.*, 2003]. Explanation of the low phase velocity anomaly with a volume of high porosity, only a small subset of which is filled by silicate melt, would also be consistent with *P* wave attenuation tomography that shows a volume of high attenuation in the uppermost ~3–5 km beneath the edifice [De Siena *et al.*, 2014].

The relatively high velocities in the 3–4 s phase velocity maps surrounding the edifice (Figure 9) are ~3.0–3.4 km/s, which is similar to slightly longer period, 5 s, phase velocities along the Cascadia arc imaged with

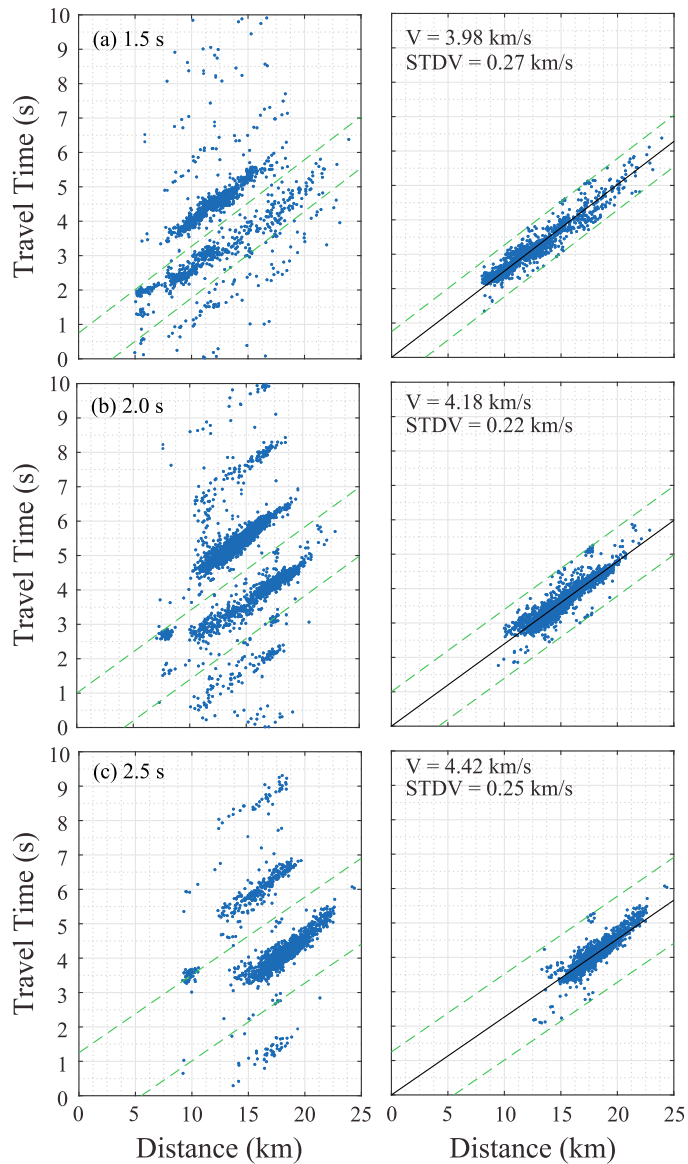


Figure 13. Phase traveltime measurements versus distance for 1.5, 2, and 2.5 s higher-mode signals satisfying the SNR and group velocity selection criterion (left). Blue dots are the measurements. Green dashed lines are the boundaries of phase ambiguity correction. The measurements applied phase ambiguity correction and one-wavelength distance selection criterion (right). The black lines fit the measurements by minimizing the misfit of traveltime. The mean and the standard deviation of the velocity are noted in the figure.

the 70 km spacing Transportable Array (Figure 1a) [Ekström, 2014]. Partially exhumed primarily Miocene age plutons on the north side of MSH are constrained by field mapping and aeromagnetic surveys [Finn and Williams, 1987; Everts et al., 1987]. The high-velocity area northwest of MSH was similarly imaged with local earthquake V_p tomography [Waite and Moran, 2009; Lees, 1992] and corresponds well with the inferred extent of the Spud Mountain pluton [Finn and Williams, 1987]. However, the full extent of the Spirit Lake pluton northeast of MSH [Everts et al., 1987] is not clearly expressed as a high-velocity feature in our phase velocity maps or prior V_p tomography [Waite and Moran, 2009]. Williams et al. [1987] also infer a shallowly buried intrusion beneath and south of MSH based on gravity data, but its boundaries are more uncertain. In general, we suggest that the higher velocities peripheral to the edifice, which are similar to regional-scale phase velocities, reflect greater proportions of low-porosity intrusive rocks in the upper crust which are not part of the active magmatic and hydrothermal system beneath the MSH.

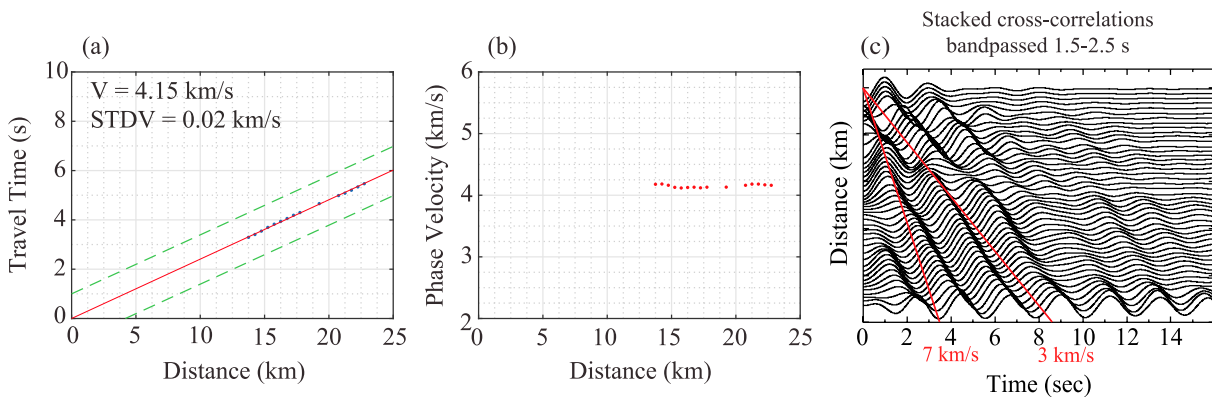


Figure 14. (a) Traveltime measurements of stacked cross correlations band passed around 2 s period (Figure 14c). Blue dots are traveltime measurements. Green dashed lines show the boundaries of phase ambiguity correction. The red lines fit the blue dots by minimizing the misfit of traveltime. The mean and standard deviation of the fitted velocity are shown. (b) Same data set as Figure 14a but uses phase velocity instead of traveltime as y axis. Both Figures 14a and 14b show that the phase velocities do not have significant variation with distance, which indicates that this signal is not body wave. (c) Stacked cross correlations in 0.5 km distance bins band passed between 1.5 and 2.5 s.

Upper crustal imaging of different volcanoes with ambient noise surface wave tomography shows a variety of results, but multiple subduction zone volcanoes have upper crustal (<5 km) low-velocity anomalies directly beneath their edifices. Using short-period surface waves from a sparser array at Uturuncu volcano in the Andes, Jay *et al.* [2012] found a similar low-velocity anomaly in the shallow crust beneath the volcanic edifice that overlaps with the most seismically active volume. Given the distribution of seismicity and evidence for magma storage at greater depths beneath Uturuncu, they interpreted the low-velocity anomaly to primarily represent a highly fractured volume containing the magma conduit and hydrothermal systems beneath the edifice. Similar results were also obtained with ambient noise surface wave tomography from a sparse array at Okmok volcano in the Aleutian Arc, where a shallow crustal low-velocity anomaly was interpreted as a combination of caldera fill underlain by a fractured magmatic conduit system [Masterlark *et al.*, 2010]. However, not all active volcanic edifices are underlain by areas of low upper crustal velocities. For example, in an active and primarily basaltic shield system at Piton de la Fournaise in the western Indian Ocean, surface wave tomography imaged a vertically elongated volume of relatively high velocities in the uppermost ~2 km beneath the summit [Brenquiere *et al.*, 2007].

4.3. Higher-Mode Signal

While imaging subsurface structure with the higher-velocity signals we observed at ~2 s period is beyond the scope of this study, we tried to evaluate if the signals are higher-mode surface waves or body waves using two approaches. In the first approach, we analyzed the relationship between phase velocity and period to determine if the signal is dispersive, which would be a clear indication of higher-mode surface waves as body waves are expected to be nondispersive. In the second approach, for a single period, we determined if the observed velocity changes as a function of distance. As body waves with longer paths tend to penetrate deeper, velocity is expected to increase with distance. Phase velocity of higher-mode surface waves, on the other hand, should not depend on distance.

Figure 13 shows all higher-mode phase traveltime measurements as a function of distance at 1.5, 2, and 2.5 s periods satisfying the SNR and group velocity selection criterion. A one-wavelength far-field selection criterion is imposed, and 2π ambiguity is corrected in the same way as performed for fundamental mode Rayleigh waves (discussed in section 2). A gradual increase of phase velocity with period is observed, indicating that the signal is dispersive and hence a higher-mode surface wave origin is likely. Figure 14 shows the relationship between 2 s phase traveltime, velocity, and distance based on stacked cross correlations with different distance bins (Figure 3c). The velocity of the ~2 s period signal does not vary with distance, which is also consistent with a higher-mode surface wave rather than a refracted body wave.

The higher-mode signal could potentially be used for tomography and is likely sensitive to deeper velocity structure than the fundamental Rayleigh waves. However, the observed higher-mode phase velocities are

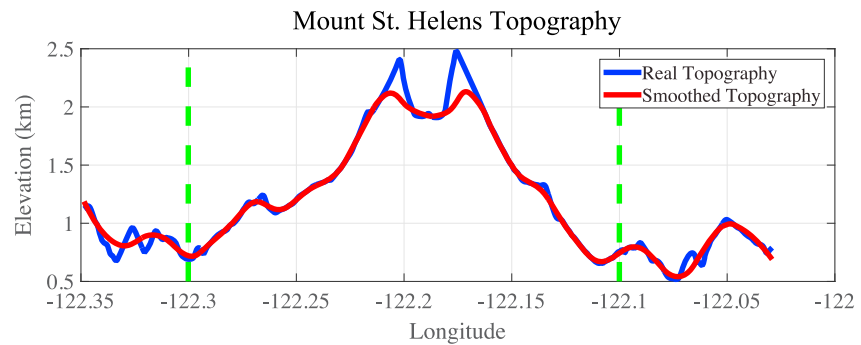


Figure 15. The topography cross section along 46.2°N in our study area (Figure 1c). The vertical exaggeration factor is about 4.5. The blue line shows the real topography, and the red line shows the smoothed topography. The two green dashed lines indicate the segment of the raypath we calculated.

considerably higher than the predicted first higher-mode phase velocities based on the 1-D reference model (section 4.1 and Figure 11b). Consequently, it is hard to determine the order of the higher mode or its depth sensitivity. Moreover, based on our beamforming analysis (Figure 7d), the noise source distribution of higher mode can be extremely uneven which means that not only good SNR measurements are limited to a particular narrow back azimuthal range but also the phase velocity measurements can be significantly biased. In light of these uncertainties we did not pursue tomography with the higher-mode signal in this study.

4.4. Topography Effect

Despite the prominent surface topography near MSH, the 2-D tomographic method we applied [Barmin *et al.*, 2001] does not consider the topography in the calculation of surface wave traveltimes. While a more sophisticated tomography method [e.g., Koulakov *et al.*, 2016] that takes the topography variation into account can potentially be applied, we do not think that topography significantly affects our results. To demonstrate that, we investigate the potential velocity bias due to topography with lateral scales larger than 5 km, assuming that smaller-scale variations will have a minimal effect on the 3–4 s Rayleigh waves (~ 10 km wavelength) used in this study.

Here we consider the extreme case where Rayleigh waves propagate along the exact surface boundary. Because surface topography will increase the raypath distance, the traveltime is expected to increase relative to a flat topography model. In that case, our tomography inversion will erroneously map such traveltime deviations into slow anomalies right beneath the areas with the greatest topographic relief. To quantify the potential effects, we chose an east-west cross section cutting through the center of MSH. (Figure 15) and calculate the length difference between a raypath following the topography and another one following a flat surface. The length of the raypath along the flat surface is about 3.2% shorter compared to the raypath along the smoothed topography. This provides an upper bound of the potential slow anomaly bias introduced by topography as long-wavelength Rayleigh waves will not necessarily follow the topography completely and the topography variation can also introduce body wave scattering that arrives earlier. We note that the $\sim 3\%$ bias is significantly smaller compared to the $\sim 20\%$ velocity contrast between slow and fast velocity anomalies observed in our tomography (Figure 9), suggesting that even in the extreme case of a path that traverses the summit crater of MSH, the topographic effects on traveltimes can contribute only a small fraction of the imaged velocity anomalies.

5. Conclusions

Ambient noise Rayleigh wave tomography results have revealed a low-velocity anomaly at shallower than 5 km below sea level beneath the MSH, which we interpret as a shallow high-porosity and fluid-rich volume beneath the volcanic edifice. A small fraction of this volume may contain silicate partial melt, but owing to the abundance of shallow seismicity and lack of supporting evidence for a large magma reservoir at such shallow depths, we suggest that much of the pore space in this volume is filled with hydrothermal fluids rather than silicate melt. This study has shown that the ambient noise tomography method can be performed to invert

for Rayleigh wave phase velocities across a dense but irregularly distributed seismic array with a short recording time. The intrinsic phase ambiguity problem of phase velocity measurements can be solved with a large number of traveltimes measurements despite the lack of a detailed reference velocity model. The challenge posed by the inhomogeneous noise source distribution during the short duration of the experiment systematically biases the Rayleigh wave phase traveltimes measurements, but it can be addressed with a correction function based on the azimuthal distribution of traveltimes residuals. Finally, we have shown a feasible way to distinguish between higher-mode and body wave signals without particle motion information, which is important for large arrays of vertical component geophones.

Acknowledgments

We thank Ivan Koulakov, Yehuda Ben-Zion, and Michael Ritzwoller for their constructive comments, which helped to improve this paper. We thank Jing Li and Gerard Schuster for their discussion on the topography effect on surface wave propagation. All waveform data used in this study can be downloaded from the IRIS Data Management Center. This work was supported by National Science Foundation (NSF) grant CyberSEES-1442665 and the King Abdullah University of Science and Technology (KAUST) under award OCFR-2014-CRG3-2300. Collection and analysis of the node array data was supported by NSF grants 1445937 (B.S.) and 1520875 (B.S.).

References

- Barmin, M. P., M. H. Ritzwoller, A. L. Levshin, M. P. B. Armin, M. H. R. Itzwiller, and A. L. L. Evshin (2001), A fast and reliable method for surface wave tomography, *Monit. Compr. Nucl. Treaty Surf. Waves*, 158(8), 1351–1375, doi:10.1007/PL00001225.
- Bedrosian, P. A., M. J. Unsworth, and M. J. Johnston (2007), Hydrothermal circulation at Mount St. Helens determined by self-potential measurements, *J. Volcanol. Geotherm. Res.*, 160(1), 137–146.
- Bensen, G. D., M. H. Ritzwoller, M. P. Barmin, A. L. Levshin, F. Lin, M. P. Moschetti, N. M. Shapiro, and Y. Yang (2007), Processing seismic ambient noise data to obtain reliable broad-band surface wave dispersion measurements, *Geophys. J. Int.*, 169(3), 1239–1260, doi:10.1111/j.1365-246X.2007.03374.x.
- Brenguier, F., N. M. Shapiro, M. Campillo, A. Nercessian, and V. Ferrazzini (2007), 3-D surface wave tomography of the Piton de la Fournaise volcano using seismic noise correlations, *Geophys. Res. Lett.*, 34, L02305, doi:10.1029/2006GL028586.
- Brocher, T. M. (2005), Empirical relations between elastic wavespeeds and density in the Earth's crust, *Bull. Seismol. Soc. Am.*, 95(6), 2081–2092, doi:10.1785/0120050077.
- Cashman, K. V. (1992), Groundmass crystallization of Mount St. Helens dacite, 1980–1986: A tool for interpreting shallow magmatic processes, *Contrib. Mineral. Petrol.*, 109(4), 431–449.
- Clyne, M. A., A. T. Calvert, E. W. Wolfe, R. C. Everts, R. J. Fleck, and M. A. Lanphere (2008), The Pleistocene Eruptive History of Mount St. Helens, Washington, from 300,000 to 12,800 Years before Present, *U.S. Geol. Surv. Prof. Pap.*, 1750, 593–627.
- Crosbie, K. (2015), Preliminary shear velocity tomography of Mt St Helens, Washington from iMUSH array, In 2015 AGU Fall Meeting, Agu.
- de Ridder, S., and J. Dellinger (2011), Ambient seismic noise eikonal tomography for near-surface imaging at Valhall, Society of Exploration Geophysicists, *The Leading Edge*, 30(5), 506–512, doi:10.1190/1.3589108.
- De Siena, L., C. Thomas, G. P. Waite, S. C. Moran, and S. Klemme (2014), Attenuation and scattering tomography of the deep plumbing system of Mount St. Helens, *J. Geophys. Res. Solid Earth*, 119, 8223–8238, doi:10.1002/2014JB011372.
- Draganov, D., X. Campman, J. Thorbecke, A. Verdel, and K. Wapenaar (2009), Reflection images from ambient seismic noise, *Geophysics*, 74(5), A63–A67, doi:10.1190/1.3273878.
- Ekström, G. (2014), Love and Rayleigh phase-velocity maps, 5–40 s, of the western and central USA from USArray data, *Earth Planet. Sci. Lett.*, 402(C), 42–49, doi:10.1016/j.epsl.2013.11.022.
- Everts, R. C., R. P. Ashley, and J. G. Smith (1987), Geology of the Mount St. Helens area: Record of discontinuous volcanic and plutonic activity in the Cascade Arc of southern Washington, *J. Geophys. Res.*, 92(B10), 10,155–10,169, doi:10.1029/JB092iB10.
- Finn, C., and D. L. Williams (1987), An aeromagnetic study of Mount St. Helens, *J. Geophys. Res.*, 92(B10), 10,194, doi:10.1029/JB092iB10p10194.
- Hansen, S. M., and B. Schmandt (2015), Automated detection and location of microseismicity at Mount St. Helens with a large-N geophone array, *Geophys. Res. Lett.*, 42, 7390–7397, doi:10.1002/2015GL064848.
- Hansen, S. M., B. Schmandt, A. Levander, E. Kiser, J. E. Vidale, G. A. Abers, and K. C. Creager (2016), Seismic evidence for a cold serpentinized mantle wedge beneath Mount St Helens, *Nat. Commun.*, 7, 13242, doi:10.1038/ncomms13242.
- Harmon, N., P. Gerstoft, C. A. Rychert, G. A. Abers, M. Salas de la Cruz, and K. M. Fischer (2008), Phase velocities from seismic noise using beamforming and cross correlation in Costa Rica and Nicaragua, *Geophys. Res. Lett.*, 35, L19303, doi:10.1029/2008GL035387.
- Hurwitz, S., K. L. Kipp, S. E. Ingebritsen, and M. E. Reid (2003), Groundwater flow, heat transport, and water table position within volcanic edifices: Implications for volcanic processes in the Cascade Range, *J. Geophys. Res.*, 108(B12), 2557, doi:10.1029/2003JB002565.
- Jay, J. A., M. E. Pritchard, M. E. West, D. Christensen, M. Haney, E. Minaya, M. Sunagua, S. R. McNutt, and M. Zabala (2012), Shallow seismicity, triggered seismicity, and ambient noise tomography at the long-dormant Uturuncu Volcano, Bolivia, *Bull. Volcanol.*, 74(4), 817–837, doi:10.1007/s00445-011-0568-7.
- Kiser, E., I. Palomeras, A. Levander, C. Zelt, S. Harder, B. Schmandt, S. Hansen, K. Creager, and C. Ulberg (2016), Magma reservoirs from the upper crust to the Moho inferred from high-resolution V_p and V_s models beneath Mount St. Helens, Washington State, USA, *Geology*, 44(6), 411–414, doi:10.1130/G37591.1.
- Koulakov, I., G. Maksotova, K. Jaxybulatov, E. Kasatkina, N. M. Shapiro, B. G. Luehr, S. E. Khrepy, and N. Al-Arifi (2016), Structure of magma reservoirs beneath Merapi and surrounding volcanic centers of Central Java modeled from ambient noise tomography, *Geochem. Geophys. Geosyst.*, 17, 4195–4211, doi:10.1002/2016GC006442.
- Lees, J. M. (1992), The magma system of Mount St. Helens: Non-linear high-resolution P-wave tomography, *J. Volcanol. Geotherm. Res.*, 53(1–4), 103–116, doi:10.1016/0377-0273(92)90077-Q.
- Lin, F. C., M. P. Moschetti, and M. H. Ritzwoller (2008), Surface wave tomography of the western United States from ambient seismic noise: Rayleigh and Love wave phase velocity maps, *Geophys. J. Int.*, 173(1), 281–298, doi:10.1111/j.1365-246X.2008.03720.x.
- Lin, F. C., M. H. Ritzwoller, and R. Snieder (2009), Eikonal tomography: Surface wave tomography by phase front tracking across a regional broad-band seismic array, *Geophys. J. Int.*, 177(3), 1091–1110, doi:10.1111/j.1365-246X.2009.04105.x.
- Lin, F.-C., D. Li, R. W. Clayton, and D. Hollis (2013), High-resolution 3D shallow crustal structure in Long Beach, California: Application of ambient noise tomography on a dense seismic array, *Geophysics*, 78(4), Q45–Q56, doi:10.1190/geo2012-0453.1.
- Lipman, P., and D. R. Mullineaux (1981), The 1980 eruptions of Mount St. Helens, Washington, *U.S. Geol. Surv.*, 1250.
- Masterlark, T., M. Haney, H. Dickinson, T. Fournier, and C. Searcy (2010), Rheologic and structural controls on the deformation of Okmok volcano, Alaska: FEMs, InSAR, and ambient noise tomography, *J. Geophys. Res.*, 115, B02409, doi:10.1029/2009JB006324.
- Rutherford, M. J., and J. D. Devine III (2008), Magmatic conditions and processes in the storage zone of the 2004–2006 Mount St. Helens dacite: Chapter 31 in *A Volcano Rekindled: The Renewed Eruption of Mount St. Helens, 2004–2006, U.S. Geol. Surv. Prof. Pap.*, 1750-31.

- Moran, S. C., J. M. Lees, and S. D. Malone (1999), *P* wave crustal velocity structure in the greater Mount Rainier area from local earthquake tomography, *J. Geophys. Res.*, *104*(B5), 10,775–10,786, doi:10.1029/1999JB900036.
- Moran, S. C., G. A. Abers, K. C. Creager, R. P. Denlinger, C. W. Ulberg, and J. E. Vidale (2014), iMUSH-aided fault-plane studies at Mount St. Helens, Washington: Evidence for magma recharge, Abstract S22C-04 presented at 2014 Fall Meeting, AGU, San Francisco, Calif.
- Mordret, A., D. Rivet, M. Landès, and N. M. Shapiro (2015), Three-dimensional shear velocity anisotropic model of Piton de la Fournaise Volcano (La Réunion Island) from ambient seismic noise, *J. Geophys. Res. Solid Earth*, *120*, 406–427, doi:10.1002/2014JB011654.
- Moschetti, M. P., M. H. Ritzwoller, F. C. Lin, and Y. Yang (2010), Crustal shear wave velocity structure of the western United States inferred from ambient seismic noise and earthquake data, *J. Geophys. Res.*, *115*, B10306, doi:10.1029/2010JB007448.
- Musumeci, C., S. Gresta, and S. D. Malone (2002), Magma system recharge of Mount St. Helens from precise relative hypocenter location of microearthquakes, *J. Geophys. Res.*, *107*(B10), 2264, doi:10.1029/2001JB000629.
- Nakata, N., J. P. Chang, J. F. Lawrence, and P. Boué (2015), Body wave extraction and tomography at Long Beach, California, with ambient-noise interferometry, *J. Geophys. Res. Solid Earth*, *120*, 1159–1173, doi:10.1002/2015JB011870.
- Nakata, N., P. Boué, F. Brenguier, P. Roux, V. Ferrazzini, and M. Campillo (2016), Body and surface wave reconstruction from seismic noise correlations between arrays at Piton de la Fournaise volcano, *Geophys. Res. Lett.*, *43*, 1047–1054, doi:10.1002/2015GL066997.
- Pallister, B. J. S., C. R. Thornber, K. V. Cashman, M. A. Clyne, H. A. Lowers, C. W. Mandeville, I. K. Brownfield, and G. P. Meeker (2008), Petrology of the 2004–2006 Mount St. Helens lava dome—Implications for magmatic plumbing and eruption triggering, a volcano rekindled renewed Erupt. Mt. St. Helens 2004–2006, U.S., *Geol. Surv. Prof. Pap.*, *1750*, 647–702.
- Poli, P., H. A. Pedersen, and M. Campillo (2012a), Emergence of body waves from cross-correlation of short period seismic noise, *Geophys. J. Int.*, *188*(2), 549–558, doi:10.1111/j.1365-246X.2011.05271.x.
- Poli, P., M. Campillo, and H. A. Pedersen (2012b), Body-wave imaging of Earth's mantle discontinuities from ambient seismic noise, *Science*, *338*(6110), 1063–1065, doi:10.1126/science.1228194.
- Roux, P., L. Moreau, A. Lecointre, G. Hillers, M. Campillo, Y. Ben-Zion, D. Zigone, and F. Vernon (2016), A methodological approach towards high-resolution surface wave imaging of the San Jacinto Fault Zone using ambient-noise recordings at a spatially dense array, *Geophys. J. Int.*, *206*(2), 980–992, doi:10.1093/gji/ggw193.
- Ruigrok, E., X. Campman, and K. Wapenaar (2011), Extraction of *P*-wave reflections from microseisms, *C. R. Geosci.*, *343*(8–9), 512–525, doi:10.1016/j.crte.2011.02.006.
- Scandone, R., and S. D. Malone (1985), Magma supply, magma discharge and readjustment of the feeding system of Mount St. Helens during 1980, *J. Volcanol. Geotherm. Res.*, *23*(3–4), 239–262, doi:10.1016/0377-0273(85)90036-8.
- Shapiro, N. M., M. Campillo, L. Stehly, and M. H. Ritzwoller (2005), High resolution surface-wave tomography from ambient seismic noise, *Science*, *307*(5715), 1615–1618, doi:10.1126/science.1108339.
- Sherrod, D. R., W. E. Scott, and P. H. Stauffer (2008), A volcano rekindled: The renewed eruption of Mount St. Helens, 2004–2006 (no. 1750), US Geological Survey.
- Snieder, R. (2004), Extracting the Green's function from the correlation of coda waves: A derivation based on stationary phase, *Phys. Rev. E Stat. Nonlin. Soft Matter Phys.*, *69*(4 Pt 2), 46610, doi:10.1103/PhysRevE.69.046610.
- Swanson, D. A., D. R. T. H. Dzurisin, R. T. Holcomb, E. Y. Iwatsubo, W. W. Chadwick, T. J. Casadevall, J. W. Ewert, and C. C. Heliker (1987), Growth of the lava dome at Mount St. Helens, Washington, (USA), 1981–1983, *Geol. Soc. Am. Spec. Pap.*, *212*, 1–16, doi:10.1130/SPE212-p1.
- Takagi, R., K. Nishida, Y. Aoki, T. Maeda, K. Masuda, M. Takeo, K. Obara, K. Shiomi, M. Sato, and K. Saito (2015), A single bit matters: Coherent noise of seismic data loggers, *Seismol. Res. Lett.*, *86*(3), 901–907, doi:10.1785/0220150030.
- Thelen, W. A., R. S. Crosson, and K. C. Creager (2008), Absolute and relative location of earthquakes at Mount St. Helens, Washington, using continuous data: Implications for magmatic processes, a volcano rekindled renewed Erupt. Mt. St. Helens 2004–2006, U.S., *Geol. Surv. Prof. Pap.*, *1750*, 71–95.
- Traer, J., P. Gerstoft, P. Bromirski, and P. Shearer (2012), Microseisms and hum from ocean surface gravity waves, *J. Geophys. Res.*, *117*, B11307, doi:10.1029/2012JB009550.
- Ulberg, C. (2015), Tomographic imaging of the magmatic system at Mount St. Helens with the iMUSH broadband array, Abstract V43B-3135 presented at 2015 Fall Meeting, AGU, San Francisco, Calif.
- Waite, G. P., and S. C. Moran (2009), V_p structure of Mount St. Helens, Washington, USA, imaged with local earthquake tomography, *J. Volcanol. Geotherm. Res.*, *182*(1–2), 113–122, doi:10.1016/j.jvolgeores.2009.02.009.
- Waite, G. P., B. A. Chouet, and P. B. Dawson (2008), Eruption dynamics at Mount St. Helens imaged from broadband seismic waveforms: Interaction of the shallow magmatic and hydrothermal systems, *J. Geophys. Res.*, *113*, B02305, doi:10.1029/2007JB005259.
- Ward, K. M. (2015), Ambient noise tomography across the southern Alaskan cordillera, *Geophys. Res. Lett.*, *42*, 3218–3227, doi:10.1002/2015GL063613.
- Williams, D. L., G. Abrams, C. Finn, D. Dzurisin, D. J. Johnson, and R. Denlinger (1987), Evidence from gravity data for an intrusive complex beneath Mount St. Helens, *J. Geophys. Res.*, *92*(B10), 10207, doi:10.1029/JB092iB10p10207.
- Yao, H., and R. D. van der Hilst (2009), Analysis of ambient noise energy distribution and phase velocity bias in ambient noise tomography, with application to SE Tibet, *Geophys. J. Int.*, *179*, 1113–1132, doi:10.1111/j.1365-246X.2009.04329.x.
- Yao, H., R. D. Van Der Hilst, and M. V. De Hoop (2006), Surface-wave array tomography in SE Tibet from ambient seismic noise and two-station analysis—I. Phase velocity maps, *Geophys. J. Int.*, *166*, 732–744, doi:10.1111/j.1365-246X.2006.03028.x.
- Yao, H., C. Beghein, and R. D. Van Der Hilst (2008), Surface wave array tomography in SE Tibet from ambient seismic noise and two-station analysis—II. Crustal and upper-mantle structure, *Geophys. J. Int.*, *173*(1), 205–219, doi:10.1111/j.1365-246X.2007.03696.x.
- Zhan, Z., S. Ni, D. V. Helmberger, and R. W. Clayton (2010), Retrieval of Moho-reflected shear wave arrivals from ambient seismic noise, *Geophys. J. Int.*, *182*(1), 408–420, doi:10.1111/j.1365-246X.2010.04625.x.
- Zigone, D., Y. Ben-Zion, M. Campillo, and P. Roux (2015), Seismic tomography of the Southern California plate boundary region from noise-based Rayleigh and Love waves, *Pure Appl. Geophys.*, *172*(5), 1007–1032, doi:10.1007/s00024-014-0872-1.